Drying Technology
An International Journal

ISSN: (Print) (Online) Journal homepage: https://www.tandfonline.com/loi/ldrt20

Impact of reattachment surface characteristics on the flow field generated by slot jet reattachment nozzle – A numerical study

Munevver Elif Asar, Mengqiao Yang & Jamal Yagoobi

To cite this article: Munevver Elif Asar, Mengqiao Yang & Jamal Yagoobi (2022): Impact of reattachment surface characteristics on the flow field generated by slot jet reattachment nozzle – A numerical study, Drying Technology, DOI: 10.1080/07373937.2022.2150862

To link to this article: https://doi.org/10.1080/07373937.2022.2150862

Published online: 02 Dec 2022.

DRYING TECHNOLOGY
https://doi.org/10.1080/07373937.2022.2150862

Impact of reattachment surface characteristics on the flow field generated by slot jet reattachment nozzle – A numerical study

Munevver Elif Asar, Mengqiao Yang, and Jamal Yagoobi

Center for Advanced Research in Drying, Worcester Polytechnic Institute, Worcester, Massachusetts, USA

ABSTRACT

Slot jet reattachment (SJR) nozzle is a novel nozzle design that overperforms the regular impingement nozzles or perforated plates for heat transfer and drying, heating or cooling applications of moist materials. The SJR nozzle is a viable design to dry fragile products such as food and paper. Mesh-type conveyor belts are commonly used in the food industry. There is a need for understanding how the SJR nozzle performs with mesh-type conveyor belts because prior studies have solely considered solid surfaces. Therefore, an extensive numerical study is performed to solve the flow field of the SJR nozzle with an exit angle of $+45^{\circ}$ on top of a mesh-type belt with and without products using *COMSOL Multiphysics*® without including heat transfer. Turbulent fluid flow is theoretically modeled using the *k*-ε turbulence model for the SJR nozzle. The numerical predictions are validated with experimental data for stationary surface. Six different cases are studied to capture the effects of the presence of products on the belt and the conveyor belt speed. Additionally, the presence of an SJR nozzle on the bottom of the belt with and without a lateral offset is studied. The mass flow rate escaping underneath the belt is compared to the total mass flow rate at the nozzle exit, shear stresses are compared at three different surface velocities, and maximum force magnitudes as product travels are reported. The results show that the flow can reattach to the product surface regardless of surface motion, but reattachment characteristics depend on product orientation with respect to the SJR nozzle. Although significant mass flow escapes through the belt, the presence of products mitigates this loss. In addition, doubling the belt speed increases the shear stresses applied by the surface and decreases the average mass flow loss. Also, an additional SJR nozzle on the bottom of the belt almost cancels this mass flow loss even when there is a lateral offset between the nozzles.

ARTICLE HISTORY
Received 18 June 2022
Revised 12 November 2022
Accepted 15 November 2022

KEYWORDS
Slot jet reattachment nozzle; SJR nozzle; nozzles; reattachment surface; moving surface; conveyor belt; flow field; mesh-type belt; turbulent flow; food drying; transient; stationary; moving mesh; dynamic mesh

1. Introduction

In recent years, governments worldwide have implemented environmental regulations to decrease various industries' energy consumption and carbon emissions.[1] Such as in the US, more than 10% of the total energy use in manufacturing is for drying.[2] This corresponds to an annual energy consumption of 1,178 TBtu or 1.178 quads.[2] Therefore, drying moist products (cookies, crackers, chips, fruits, etc.) is a critical process in manufacturing[2], where air-impinging nozzles are generally used. Tsotsas and Mujumdar[3] reviewed the state-of-the-art and modern drying technologies in their book.

Impinging jets are extensively used in various industrial applications, and their performance has been analyzed for several decades. Martin[4] presented an extensive survey focusing on engineering applications and empirical equations for conventional round and slot nozzles for both single and array of nozzles. More and notable studies on the impinging jets were conducted by various researchers to examine crossflow effects, jet orientation (oblique jets) and surface characteristics[5]; nozzle-to-plate spacing, nozzle geometry[6]; Reynolds number[7]; chamfering of nozzles[8]; elliptical nozzle[9]; and pulsed impingement[10,11]. Ekkad and Singh[12] reviewed jet impingement heat transfer methods in their recent work. Katti et al.[13] analyzed inline jet (ILJ)'s nozzle-to-surface spacing and the effect of the Reynolds number. They identified three regions on the target surface: stagnation, transition and wall jet. Shiravi et al.[14] presented various cases of *k*-ε turbulence models for single and multiple jets with and without cross flow. They found that high Reynolds number

CONTACT Munevver Elif Asar masar@wpi.edu 100 Institute Road Worcester, MA 01609, USA

turbulence (e.g., Standard k-ε) accurately predicted the flow field but did not accurately predict the heat transfer to the impingement surface.

There are various studies on jet impingement drying on finite-size substrates. Liu et al.[15] studied hot air impingement drying of broccoli florets. They found that the pretreatment method called blanching can increase the drying rate. By artificial neural network, Liu et al.[16] predicted energy and exergy of mushroom slices during drying via hot air impingement. Ai et al.[17] studied the effect of hot air impingement drying of *Amomum villosum* fruit using an array of ILJ nozzles. They reported the favorable drying conditions of air temperature and velocity based on quality. Boy et al.[18] experimentally and numerically examined digestate drying with an array of SJ nozzles and determined the essential characteristics for optimizing the drying process. Khatir[19] presented a methodology for predicting optimum conditions to obtain maximum energy efficiency in a commercial baking oven using an array of IJ nozzles by combining heat transfer, airflow and a bread baking model.

Nevertheless, these impinging nozzles exert high pressures on the impinging surface, which is a major drawback for drying fragile products. For drying fragile products, the mass flow rate must be reduced to avoid high pressures on the surface of the products, which leads to reduced heat and mass transfer performance.[20] One way to enhance the energy efficiency of drying without causing high surface pressures is using air impingement nozzles such as the slot jet reattachment (SJR) nozzle.

Slot jet reattachment (SJR) nozzle stems from radial jet impingement (RJR) nozzle because first, a nozzle design called radial jet impingement (RJR) nozzle was introduced where the flow is diverted radially using a plate at the nozzle exit.[21,22] RJR nozzle creates a turbulent reattachment ring on the target surface with high heat transfer characteristics.[21] RJR nozzle provided up to 60% and 50% higher local and area-averaged heat transfer coefficients, respectively, compared to ILJ nozzle.[23] Moreover, with the RJR nozzle, the pressure exerted on the target surface, and the reattachment location can be controlled by changing the flow exit angle.[23,24] The pressure exerted could be positive, negative or zero to provide gentle drying, heating, or cooling.[23,24]

Later, SJR nozzles were designed as an extension of RJR nozzles and developed by Page and Seyed-Yagoobi.[25] SJR nozzles outperform the slot jet (SJ) nozzle in heat transfer as it generates regions with high heat transfer coefficients on the turbulent reattachment zones at the two sides of the nozzle. Narayanan et al.[26] and Alam et al.[27] extensively studied the drying characteristics of SJR nozzles with various nozzle exit angles. Farzad et al.[28] experimentally studied heat transfer characteristics of SJR nozzle (with $+20^{\circ}$ and $+45^{\circ}$) with RJR (with $+45^{\circ}$), ILJ and SJ nozzles using potato chips and apples on a stationary set-up. They found all SJR and RJR nozzles studied outperformed the baseline nozzles for all three criteria of identical air mass flow rate, fluid flow power, and peak surface pressure.

Furthermore, Farzad and Yagoobi[29] used SJR (with $+20^{\circ}$ and $+45^{\circ}$) and baseline SJ nozzles to dry moist cookie doughs. They reported that SJR + 45° and SJR + 20° showed up to 45% and 44% enhancement in drying rates compared to the baseline under identical air mass flow rate criterion, respectively. Nienke et al.[30] used oblique twin nozzle designs that are similar to SJR nozzle designs with negative (convergent nozzle, -45°) and positive angles (divergent nozzle, $+45^{\circ}$). They conducted an experimental and numerical investigation for industrial thin film drying applications. They concluded that the convergent nozzle displays a higher heat transfer coefficient than the divergent nozzles.

The target surface moves relative to the nozzles for continuous production in most process industries to achieve high throughput. Therefore, the effect of surface (i.e., belt) motion on the performance of nozzles needs to be analyzed. For SJ and IJ nozzles, jet impingement on a moving flat surface has been numerically and experimentally studied by several researchers. Zumbrunnen[31] studied the stagnation region of laminar and planar jets with moving surfaces and formulated similarity solutions for mass and energy conservation equations. Shah[32] conducted a numerical study using the *SST* k-ω turbulence model for an array of IJ impinging on a flat moving surface with a surface-to-jet-velocity ratio (r) of 0.25-2.0 and three different jet-to-jet spacing of $2D$, $4D$ and $6D$ (D: jet diameter). They found that for a single jet, average Nusselt number remains almost constant for $0 \leq r \leq 0.75$ and then increases significantly at $r \geq 0.75$, but this increase is smooth for multiple jets. Chen et al.[33] numerically studied convective heat transfer of an array of inline jets on a moving plate. They reported that neglecting surface motion can result in overestimating heat transfer and stressed the importance of including surface velocity effects. Chattopadhyay and Saha[34] numerically studied the turbulent flow and heat transfer from SJ impinging on

a moving plate using large eddy simulation technique. They reported turbulent kinetic energy, the production rate of turbulent kinetic energy, and Reynolds stresses for various surface velocities. In another study, Chattopadhyay[35] examined the effect of surface motion on transport processes due to circular impinging jets. He found that surface motion affects the transport process adjacent to the target surface, leading to decreased (10-20% reduction compared to stationary surface) but more uniform heat transfer for both laminar and turbulent regimes. Similarly, array of round jets impinging on a moving surface was investigated in all flow regimes (laminar, transitional and turbulent).[36] Huang et al.[37] conducted a numerical study of a turbulent SJ nozzle with a moving plate inside a rectangular duct. They found that the Nusselt number was higher when the surface velocity and jet flow were in the same direction and vice versa. Few studies have experimentally investigated SJ and IJ nozzles' heat transfer, such as Raju et al.[38] They reported that the heat transfer coefficients of an impinging jet increased steeply with belt speed to a maximum value and remained almost constant for other higher belt speeds, over the belt speed range of 0.15 to 5.5 m/s. In addition, Senter and Solliec[39] used PIV for SJ and showed that at a given surface-to-jet velocity ratio, flow field patterns were independent of Reynolds numbers for 5,300-10,600. There are other studies that investigated SJ heat transfer experimentally, e.g.,[38] In addition, some studies focused on drying/baking finite-sized moist food substrates while traveling on a conveyor belt. For example, Chen et al.[40] modeled radio frequency heating of food, Kangarluei[41] modeled an industrial biscuit baking oven by utilizing the finite difference method, El-Mesery and Mwithiga [42] conducted apple slice drying experiments using combined infrared and hot air heating. Baik et al. studied cake baking in a tunnel type multi-zone industrial ovens and they characterized baking conditions[43] and product quality.[44] Similarly, Xue and Walker[45] and Zareifard et al.[46] studied cake baking in an electrically heated air impingement oven and reported humidity effects on final product quality and the effect of convection heat flux, respectively.

Regarding the SJR nozzle, Farzad and Yagoobi[47] combined SJR and SJ nozzles with a moving reattachment surface for the first time and numerically studied the impact of reattachment surface velocity with a solid moving plate using the k-ε turbulence model for various surface-to-jet velocity ratios from 0 to 1.5. They reported that SJ nozzles' flow fields were greatly affected by the surface-to-jet velocity ratios (u^*) above $u^*=0.5$ such that SJ nozzle's flow detached from the surface. They also showed that SJR + 45° and SJR + 20° nozzle flow resisted this detachment at $0\leq u^*<1$ because of the indirect flow impingement due to the nozzle angle. In addition, they found that the flow impingement locations move forward in the surface velocity direction for non-zero velocities compared to that of the stationary surface. Later, Farzad and Yagoobi[48] incorporated heat transfer into their analysis under a laminar flow regime. They showed that SJR + 45 nozzle yields a 54% higher average convective heat transfer coefficient compared to SJ nozzle with moving flat plate velocity of $u^*=0.5$ under identical air mass flow rate criterion.

Mesh-type conveyor belts are commonly used in the food and other industry sectors, and there is a need for understanding how the SJR nozzle performs with mesh-type conveyor belts. Prior studies have only considered solid surfaces. For the first time, a numerical study is performed to solve the turbulent flow field of the SJR nozzle on a moving perforated reattachment surface. This study requires challenging numerical analysis incorporating various moving complex geometries to account for belt movement with and without products. This study is only concerned with the flow field and not the heat transfer performance of the SJR nozzle. However, it is predicted that if the SJR flow reattachment occurs and there is little or no mass flow bleeding under the belt, the SJR nozzle's heat transfer performance on that perforated surface would be similar to that of with a solid surface. Therefore, this study aims to analyze the transient flow field of the SJR nozzle by various case studies to understand the effect of surface perforation, surface velocity (including zero velocity cases), the impact of product's presence and nozzle arrangement to the flow field of SJR nozzle (whether flow reattachment occurs and how much flow bleeds under the belt due to surface perforation).

1.1. Slot jet reattachment nozzle

Figure 1 displays the schematic of the SJR nozzle impinging on a solid flat plate. SJR nozzle displays different flow behaviors than regular IJ nozzles. Instead of a stagnation region at $x=0$, the SJR nozzle's flow occurs away from the nozzle center in a relatively larger turbulent reattachment region resulting in high heat and mass transfer characteristics. Figure 1 also shows the recirculation regions where the local heat transfer coefficient is lower than that of

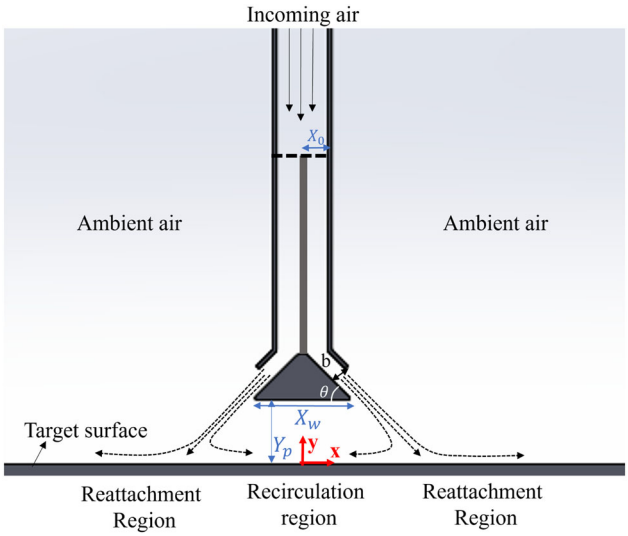

Figure 1. Schematic of slot jet reattachment nozzle.

the reattachment region. Reynolds number of SJR nozzle is calculated with Eq. (1):

$$Re = \frac{\rho\ u_e\ D_h}{\mu} \tag{1}$$

where U_e, ρ and μ correspond to average nozzle exit velocity, the density of air and dynamic viscosity of air. D_h is the hydraulic diameter of the SJR nozzle and corresponds to $2b$ or twice the nozzle exit opening.

2. Theoretical method

2.1. Governing equations

The current study is only concerned with the flow field of the SJR nozzle and does not solve the energy rate equation to account for a drying, heating, or cooling process. Therefore, the flow field is studied at 293.15 K and 1 atm ambient air conditions with the exact temperature at the nozzle exit. Flow field results are obtained using *COMSOL Multiphysics*®[49] with the k-ε turbulence model based on Reynolds-Averaged Navier Stokes (RANS) Equations for incompressible and Newtonian flow. RANS equations with Boussinesq eddy-viscosity approximation are given in Eq. (2) and Eq. (3), ignoring the body force term. k-ε turbulence model is based on eddy (or turbulent) viscosity (μ_T) which is estimated with Eq. (4) where k is the turbulent kinetic energy. The transport equations for k and ε are given in Eq. (5) and Eq. (6), where the production term, P_k, is shown in Eq. (7). The empirical constants in below equations are: $C_{\epsilon 1} = 1.44$ $C_{\epsilon 2} = 1.92$ $C_\mu = 0.09$ $\sigma_k = 1$ and $\sigma_\varepsilon = 1.3$. All computations are performed by *COMSOL Multiphysics*® 6.0.[49]

$$\rho\frac{\partial \boldsymbol{U}}{\partial t} + p\boldsymbol{U}\ .\ \nabla\boldsymbol{U} = -\nabla \mathrm{P} + \ \nabla\ .\left[\ \left(\mu + \mu_T\right)\ \left(\nabla\mathbf{U} + (\nabla\mathbf{U})^T\right)\right] \tag{2}$$

$$\rho\nabla\ .\ \boldsymbol{U} = 0 \tag{3}$$

$$\mu_T = \rho C_\mu \frac{k^2}{\varepsilon} \tag{4}$$

$$\frac{\partial k}{\partial t} + \rho(\boldsymbol{U}\ .\ \nabla)\mathrm{k} = \ \nabla\ .\left[\ \left(\mu + \frac{\mu_T}{\sigma_k}\right)\ \nabla\mathrm{k}\right] + P_k - \rho\varepsilon \tag{5}$$

$$\rho\frac{\partial \epsilon}{\partial t} + \rho(\boldsymbol{U}\ .\ \nabla)\varepsilon = \nabla\ .\left[\ \left(\mu + \frac{\mu_T}{\sigma_\varepsilon}\right)\ \nabla\varepsilon\right] + C_{\varepsilon 1}\frac{\epsilon}{k}P_k - C_{\varepsilon 2}\rho\frac{\epsilon^2}{k} \tag{6}$$

$$P_k = \mu_T\left[\nabla\boldsymbol{U} : \left(\nabla\boldsymbol{U} + (\nabla\boldsymbol{U})^{\boldsymbol{T}}\right)\right] \tag{7}$$

2.2. Wall functions

The flow near the walls is very different from the free stream, which means that the assumptions used to derive the k-ε turbulence model (i.e., high enough Re assumption) are not valid near the walls.[50] Therefore, analytical expressions (wall functions) are used to treat the flow field near the walls. When utilizing wall functions in *COMSOL Multiphysics*®[49], it is assumed that there is a small gap (δ_w) between the physical wall and the computational domain, called theoretical wall liftoff. Nondimensional version of δ_w (δ_w^+) is shown in Eq. (8) where u_τ is friction velocity and defined by Eq. (9), h is the height of the mesh adjacent to the wall, and tangential dimensionless velocity (u^+) is given by Eq. (10). δ_w^+ is computed using Eq. (11). The first term on the right-hand side of Eq. (11) stems from law of the wall and the second term is the distance from the wall (y^+) where the logarithmic layer would meet the viscous sublayer if no buffer layer existed. By definition, $\delta_w = h/2$ when $\delta_w^+ > 11.06$. If $\delta_w^+ < 11.06$, δ_w can become larger than $h/2$.

$$\delta_w^+ = \frac{\delta_w \rho\ u_\tau}{\mu} \tag{8}$$

$$u_\tau = \max\left(C_\mu{}^{0.25}\sqrt{k}\ ,\ \frac{\|\boldsymbol{U}\|}{u^+}\right) \tag{9}$$

$$u^+ = \frac{1}{\kappa_v}\log\left(\delta_w^+\right) + B \tag{10}$$

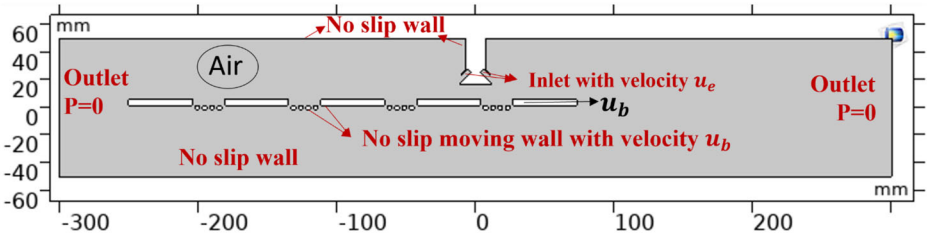

Figure 2. Computational domain and boundary conditions. (Geometry of reattachment surface varies depending on Case Studies).

$$\delta_w^+ = \max\left(\frac{h\rho C_\mu^{0.25}\sqrt{k}}{2\mu}\ ,\ 11.06\right) \tag{11}$$

The boundary condition at the wall for velocity is a non-penetrating wall defined with Eq. (12). The shear stress condition at the wall is given by Eq. (13), where σ is viscous stress tensor and is given in Eq. (14).

$$\boldsymbol{U}\ .\ \boldsymbol{n} = 0 \tag{12}$$

$$\boldsymbol{n}\ .\ \sigma - (\boldsymbol{n}\ .\ \sigma\ .\ \boldsymbol{n})\boldsymbol{n} = \ -\rho\ u_\tau \frac{\boldsymbol{U}}{u^+} \tag{13}$$

$$\sigma = \mu\ (\nabla \boldsymbol{U} + (\nabla \boldsymbol{U})^T) \tag{14}$$

In addition, the turbulent kinetic energy at the wall and turbulent dissipation rate satisfy Eq. (15) and Eq. (16), respectively. More information about the wall treatment can be found in *COMSOL* documentation.[50]

$$\boldsymbol{n}\ .\ \nabla k = 0 \tag{15}$$

$$\varepsilon = \frac{C_\mu^{0.75} k^{1.5}}{\kappa_v \delta_w} \tag{16}$$

2.3. Geometry and boundary conditions

Based on the literature[26–29,47,48,51,52], the SJR nozzle parameters are selected for the optimal conditions regarding heat transfer/drying operations. Therefore, for the selected fixed SJR nozzle geometry and spacing between the nozzle and the surface, the computational domain and boundary conditions are illustrated in Figure 2. The domain contains one or two SJR + 45° nozzle(s) and a conveyor belt with or without product. Note that the reattachment surface characteristics and the SJR nozzle placements depend on the case study. However, all the cases have two pressure ($P = 0$) outlets on the left and right, velocity inlet boundary conditions at nozzle exits, and no-slip boundary conditions on the rest of the walls. For transient cases with belt movement, the prescribed wall velocity of belt and products are non-zero; otherwise, the walls have no-slip condition with zero velocity. The top and bottom walls' being no-slip walls do not necessarily affect the flow field. In addition, the size of the computational domain shown in Figure 2 is chosen so as not to alter the flow field. Moreover, since the stationary study with the conveyor belt (Case 1) is symmetric about the $x = 0$ axis, a symmetry boundary condition is applied at $x = 0$, and only half of the domain shown in Figure 2 is used for the sake of computational cost reduction. The details of the case studies are discussed in the "Case Studies" section.

The dimensions of the nozzle, conveyor belt and products (e.g., food substrates) are given in Figure 3. The conveyor belt dimensions correspond to a simplified version of a mesh-type belt given in Figure 3e. For the computation of an SJR nozzle on top of the belt with products, the belt geometry is simplified so that the products act as if they are a part of the belt (see Figure 3c). However, this modification is not applied when the cases where there are SJR nozzles on both sides (top and bottom) of the belt as shown in Figure 3d.

3. Numerical methodology

The flow field or the computational domain is filled with free triangular meshes and eight layers of boundary layer mesh to resolve the region near the walls. As an example, Case 2's mesh grid representation is given in Figure 4 where boundary layer meshes are shown near the products and belt pieces. For the transient studies where the conveyor belt is moving, the domain is set as deforming to allow for moving walls with prescribed velocity. Transient cases require a moving or dynamic mesh in the domain since there is a moving wall. The set of governing equations and boundary conditions discussed above were solved with segregated approach[53] and using parallel sparce direct solver (PARSIDO)[54] embedded in *COMSOL Multiphysics®*.[49] The software was run using an *Intel(R) Xenon(R) Gold* 6148 CPU with 20 cores, 40 logical processors and 384 GB RAM. The computations took ~10-40 hours for moving belt cases whereas it was faster for stationary cases (~20-60min). In addition, transient studies are conducted with a maximum time step size of 0.1 ms. Mesh-independency analysis was conducted by increasing the

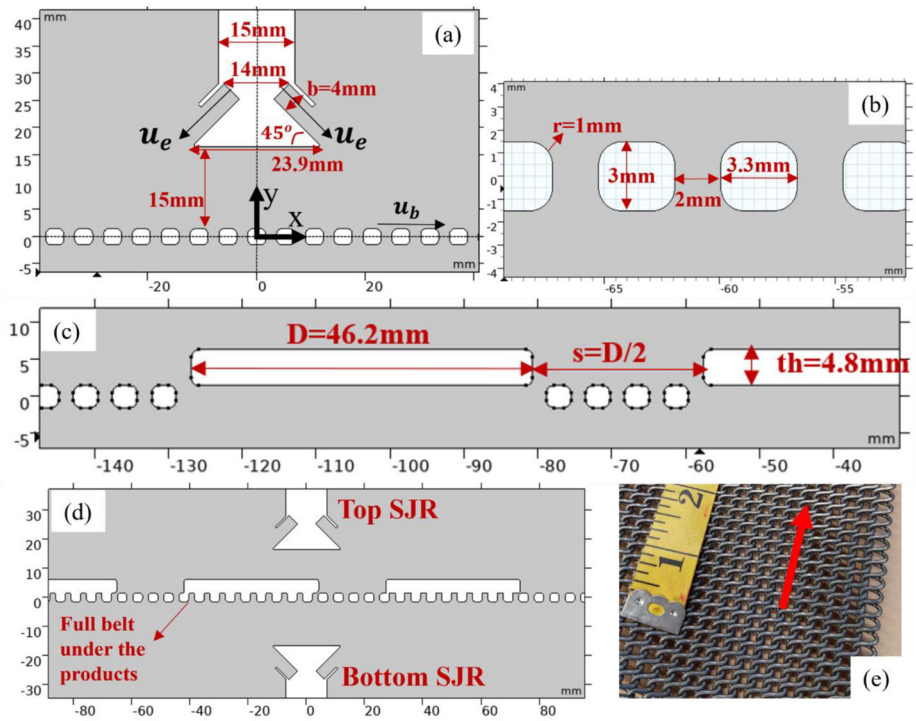

Figure 3. Geometry dimensions (a) SJR nozzle; (b) simplified version of conveyor belt in (e); (c) product and product placement; (d) Zoomed-in domain to show geometry of the cases where additional bottom SJR nozzle is studied, visual showing no-offset case between the two nozzles; (e) a mesh type conveyor with an arrow showing the belt velocity direction with a scale (in inches).

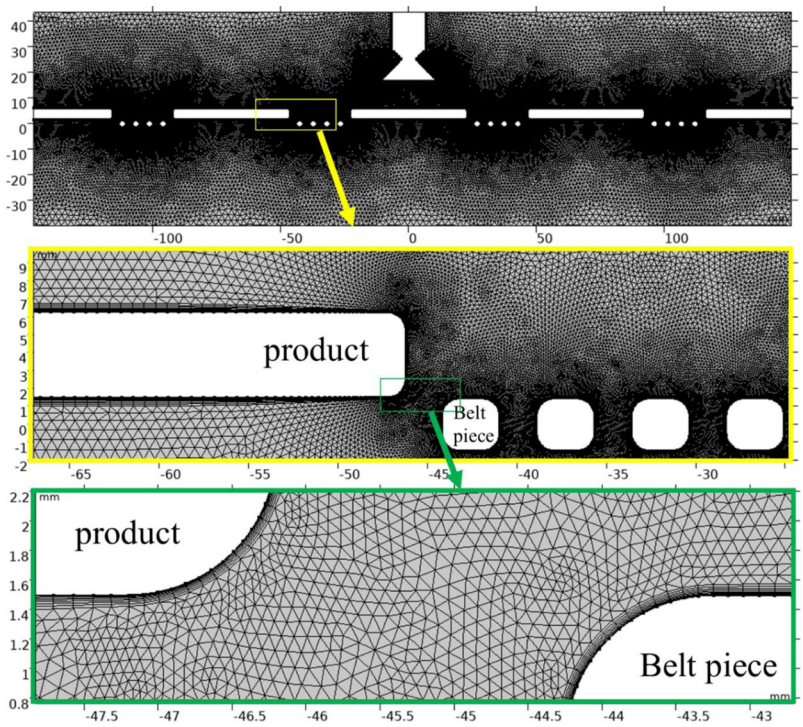

Figure 4. Mesh grid representation of Case 2; zoomed-in visuals for clarity showing triangular meshes and boundary layer meshes.

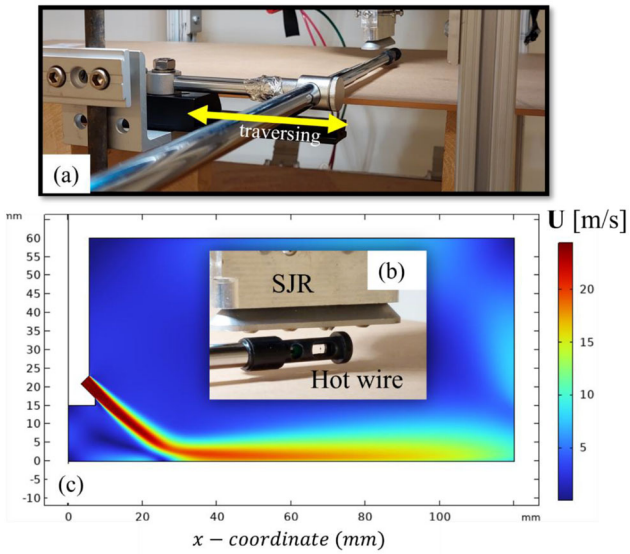

Figure 5. (a) A section of experimental set-up of validation experiments showing SJR nozzle, solid plate and hot-wire probe attached to a traverse, (b) Hot-wire and SJR nozzle close-up photo; (c) numerical domain matching with experiments and numerical results for exit velocity of 24 m/s.

element number until the *mass flow rate ratio* errors were within 1%. The results with a 0.01% tolerance convergence criterion are given in the "Results and Discussion" section.

4. Validation of numerical results

Numerical results are validated by hot-wire air velocity measurements taken from an experimental set-up housing an SJR nozzle with a 45° exit angle on a stationary flat plate. Compressed air at 820 kPa (differential) was directed to a pressure regulator and rotameter to control and measure the air volumetric flow rate, respectively. The regulated compressed air then connects to the SJR nozzle, as seen in Figure 5a and b. The flat plate was placed 15 mm away from the bottom of the nozzle, identical to all cases considered in this study and similar to the distance used in Farzad et al.[51] An *OMEGA* hot-wire anemometer capable of measuring 0-25 m/s was placed 6 mm above the plate. As seen in Figure 5a, the hot-wire was attached to a precise railing system with 1 mm marks and manually traversed to obtain the desired air velocity measurements within the hot-wire probe range. The experimental data were collected for nozzle exit velocities of 12 m/s and 24 m/s and repeated ten times for each case. The standard deviation of the results was 11% and 10% for 12 m/s and 24 m/s cases, respectively.

The numerical results for 24 m/s nozzle exit velocity can be seen in Figure 5c. The numerical study has a symmetry boundary condition at $x = 0$, where the x-axis is a stationary no-slip wall. In addition, numerical and experimental results are plotted in Figure 6 for comparison. Both numerical and experimental results follow a typical SJR nozzle flow field. Experimental results reasonably follow the numerical predictions for both air velocities. The experimental results vary from the numerical results near the nozzle (close to $x = 0$) because the casing around the hot-wire affects the results since it is a tight gap, which is expected. Note that there is no measurement data around $x = 0$ because the hot-wire did not fit underneath the nozzle.

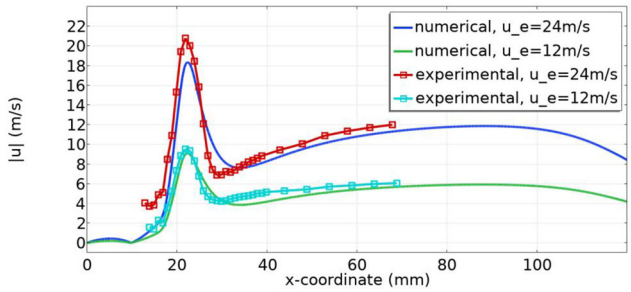

Figure 6. Comparison of experimental data vs numerical data for validation. Air velocity magnitude in x direction at y = 6mm vs x-coordinate (x = 0, center of nozzle).

5. Case studies

In this work, six case studies are presented. A summary of them is given in Table 1. Cases 1 and 2 are stationary (thus, steady state) cases containing mesh-type conveyor belts without and with products, respectively. The rest of the cases are transient, and the reattachment surface moves with a specified velocity. The transient cases have a surface-to-jet flow velocity ratio, $u^* = u_b/u_e$, where u_b is belt velocity and u_e is the air velocity at the nozzle exit and is 8 m/s for all cases. With a nozzle exit spacing $b = 4$mm, the Reynolds number at the jet exit corresponds to 4,300 at 293.15 K and 1 atm.

The effect of belt speed on the flow field is explored in Case 5, where u^* is doubled. Moreover, Case 6 is to investigate the addition of an SJR nozzle at the bottom of the belt. Case 6 is studied with zero and 6 mm lateral offset between the two SJR nozzles. The offset case (Case 6.2) is studied because it may not be realistic to achieve perfect symmetry in an actual industrial application.

6. Results and discussions

This study aims to understand the impact of the reattachment surface on the performance of the SJR nozzle. It is predicted that if the SJR flow reattachment occurs and there is little or no mass flow

Table 1. Summary of case studies.

Case studies	Model	u^*	Products	Bottom SJR Nozzle
Case 1	Stationary	0	No	No
Case 2	Stationary	0	Yes	No
Case 3	Transient	0.1	No	No
Case 4	Transient	0.1	Yes	No
Case 5	Transient	0.2	Yes	No
Case 6	Transient	0.1	Yes	Yes

bleeding under the belt, the SJR nozzle's heat transfer performance on that perforated surface would be similar to that of with solid surface. Therefore, evaluating how the flow reattaches and how much of the flow escapes through the belt is crucial. Thus, a non-dimensional parameter called *mass flow rate ratio* is introduced as given in Eq. (17), where the velocity in the y-direction (v) is integrated along 89 mm distance at $y=0$ location (middle of belt). The integration limits are selected to focus on the effect of one SJR nozzle since there would be an array of SJR nozzles in an actual application instead of a single nozzle. The spacing between the SJR nozzles can be 89 mm, similar to the array of SJR($+45^{\circ}$) nozzles studied in Farzad et al.[51] with the same nozzle exit opening of 4 mm. The higher the *mass flow rate ratio*, the greater the airflow bleeding through the belt and the lower the SJR nozzle's drying, heating, or cooling effectiveness.

$$\begin{aligned} &\textit{Mass Flow Rate Ratio} \\ &= \frac{\textit{total mass flow escaping under the belt}}{\textit{total mass flow at the nozzle exit}} \\ &= \frac{-\int_{x=-44.5mm}^{x=44.5mm} v\ dx}{2bu_e} \end{aligned} \tag{17}$$

6.1. Case 1: Stationary study without samples on conveyor belt ($u^*=0$)

The 2-D flow field of Case 1 and velocity at the y-coordinate at the middle of the belt are given in Figure 7. Case 1 shows a visible reattachment region, but some of the mass flow penetrates through the belt and escapes, as expected. The *mass flow rate ratio* is calculated using the velocity plotted in Figure 7b and Eq. (17) and is 61.6%. Note that the belt velocity is not considered because Case 1 is a stationary or steady-state study.

6.2. Case 2: Stationary study with samples on conveyor belt ($u^*=0$)

Case 2 is similar to Case 1 but contains 4-5 products on the belt. There are three product locations studied with respect to the nozzle. 2-D flow field and v at

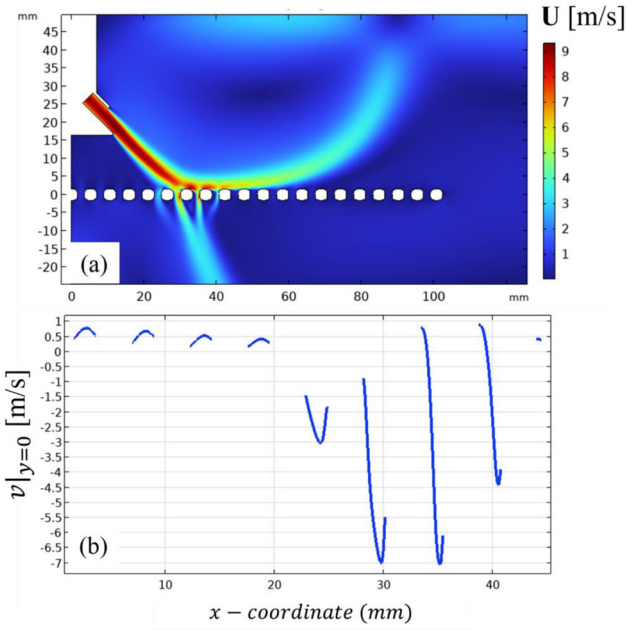

Figure 7. Case 1, u^*=0- (a) Velocity magnitude (zoomed-in domain), (b) Velocity vector in y- component of velocity vector at y = 0.

$y=0$ are shown in Figure 8 for all cases. Case 2.1 has five products, and the third product is right below the nozzle. There is no visible reattachment, and 65.2% of the flow escapes through the belt, and the rest deflects up from the corner of the products. Case 2.2 also has five products, but only the right-half of the third product is directly underneath the nozzle. In this case, most of the flow reattaches on the surface of the products, and 20.3% escapes from the belt. In Case 2.3, there are four products in total, and the middle two products are located symmetrically with respect to the nozzle. In this case, the flow reattaches on the surface of the products, similar to Case 2.2 but only 12% is lost from the belt. Note that Case 2.1 and Case 2.3 are geometrically symmetric and have symmetric boundary conditions about the y-axis, but the velocities shown in Figure 8d are slightly asymmetric. Crawford and Knobloch[55] studied the symmetry and symmetry-breaking bifurcations in fluid dynamics and stated that fluid-dynamic models can yield solutions with less symmetric than the governing equations. Oberlack[56] stated that "[…] many two-equation turbulence models [such as k-ε turbulence model] needed to use damping functions close to solid walls, and these are in fact symmetry breaking with respect to rotational and translational invariance". Therefore, the slight asymmetry of the velocity results is expected to be caused by the turbulence model. Also, the impact of the numerical asymmetry on the resultant *mass flow rate ratio* is negligible.

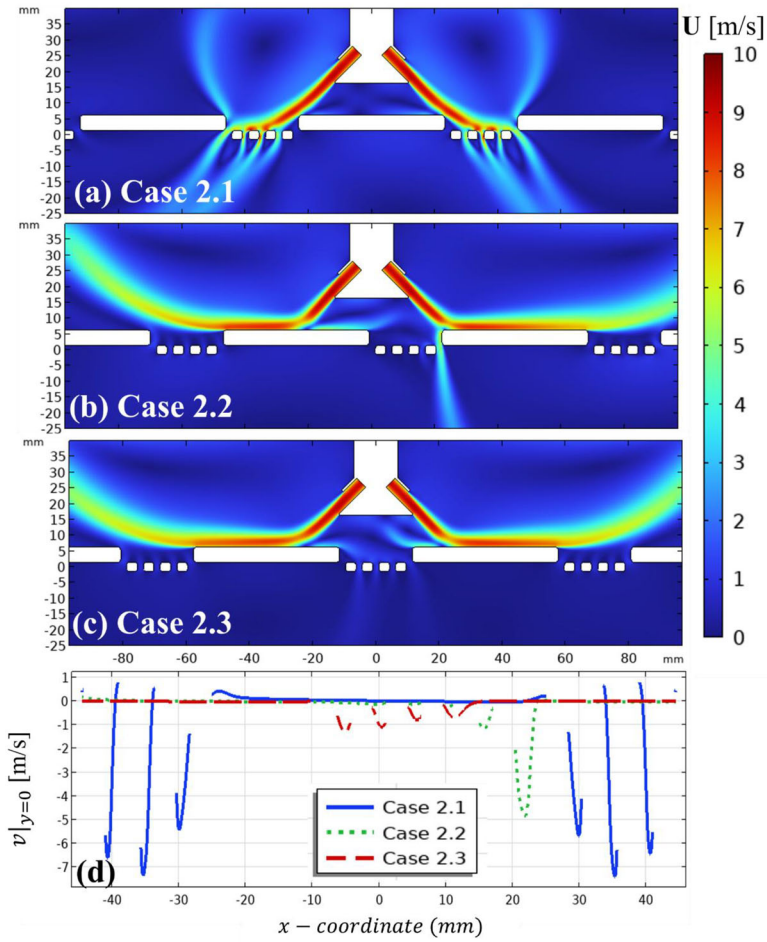

Figure 8. Case 2, u^*=0- (a-c) Velocity magnitude results with three different product locations (zoomed-in, not showing whole computational domain for clarity); (d) y- component of velocity vector for all product locations of Case 2.

6.3. Case 3: Transient study with moving conveyor belt (u^*=0.1)

The transient study starts at $t = 0$s with a zero-velocity initial condition on the computational domain. The belt velocity rises from 0 to 0.8 m/s in 0.5 ms, and the flow at the nozzle exit reaches the belt around $t = 10$ms. 2-D flow fields are plotted in Figure 9a–c for three different times. The instantaneous *mass flow rate ratio* is calculated and shown in Figure 9d while the belt is underneath the nozzle (t = 70-100ms). The *mass flow rate ratio* averages 71% and fluctuates due to the periodical void regions on the reattachment surface. Its local minimum and maximum change slightly with respect to time due to the belt moving from one side to another. Overall, the velocity of the moving belt affects the characteristics of the flow field.

6.4. Case 4: Transient study with moving conveyor belt and products (u^*=0.1)

The transient study starts as described in Case 3. In Case 4, there are five products, and the middle product is of interest. While the middle product passes under the nozzle, the 2-D flow field at five instances is shown in Figure 10a–e, where each instance shows a different product orientation. In addition, the *mass flow rate ratio* is given in Figure 10f. The *mass flow rate ratio* varies between 1.8-44%, where the minimum is reached when the flow reattaches on product surfaces, as displayed in Figure 10e. This behavior is similar to the stationary study (Case 2). On the other hand, the maximum *mass flow rate ratio* is at $t = 37$ms and 122 ms. Figure 10d shows the product position at $t = 122$ms, leading to the highest mass flow escape through the belt. At $t = 37$ms, the flow field is very similar to $t = 122$ms, but it is not shown here. Overall, the average *mass flow rate ratio* over one period is 22.2%.

In addition, the effect of shear stress in the flow field due to surface movement can be seen from the flow streaks on both sides of the nozzle. For instance, the thickness of the flow streak (see Figure 10) is thicker on the left-hand side than on the right-hand side due to the higher shear stress in the x-direction applied by the moving surface. A detailed analysis of shear stress is given in the following subsection.

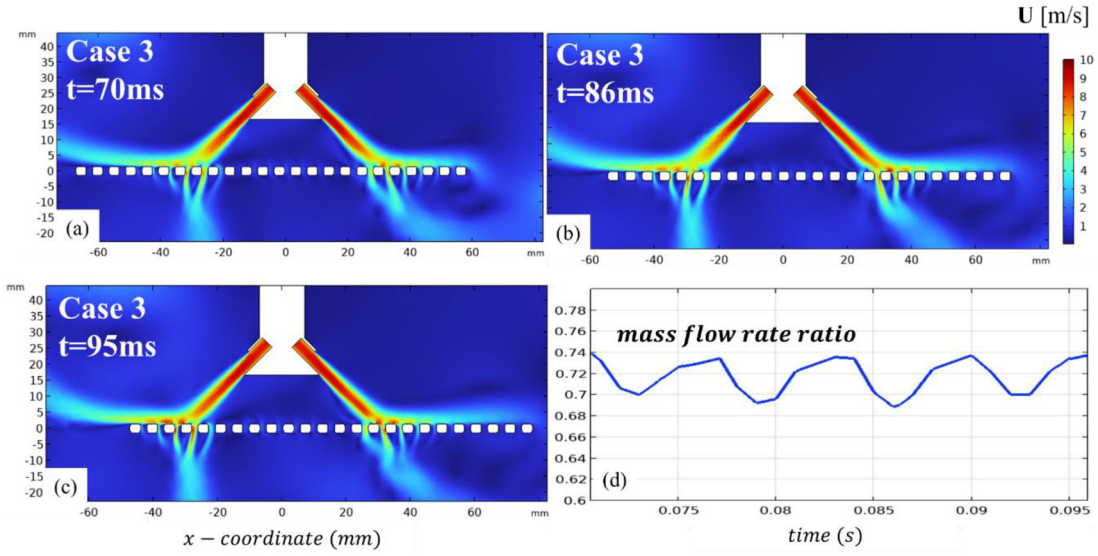

Figure 9. Case 3, u^*=0.1- (a-c) Flow field at t = 70ms, 86 ms and 95 ms, respectively; (d) *Mass flow rate ratio* while conveyor belt passes through the nozzle.

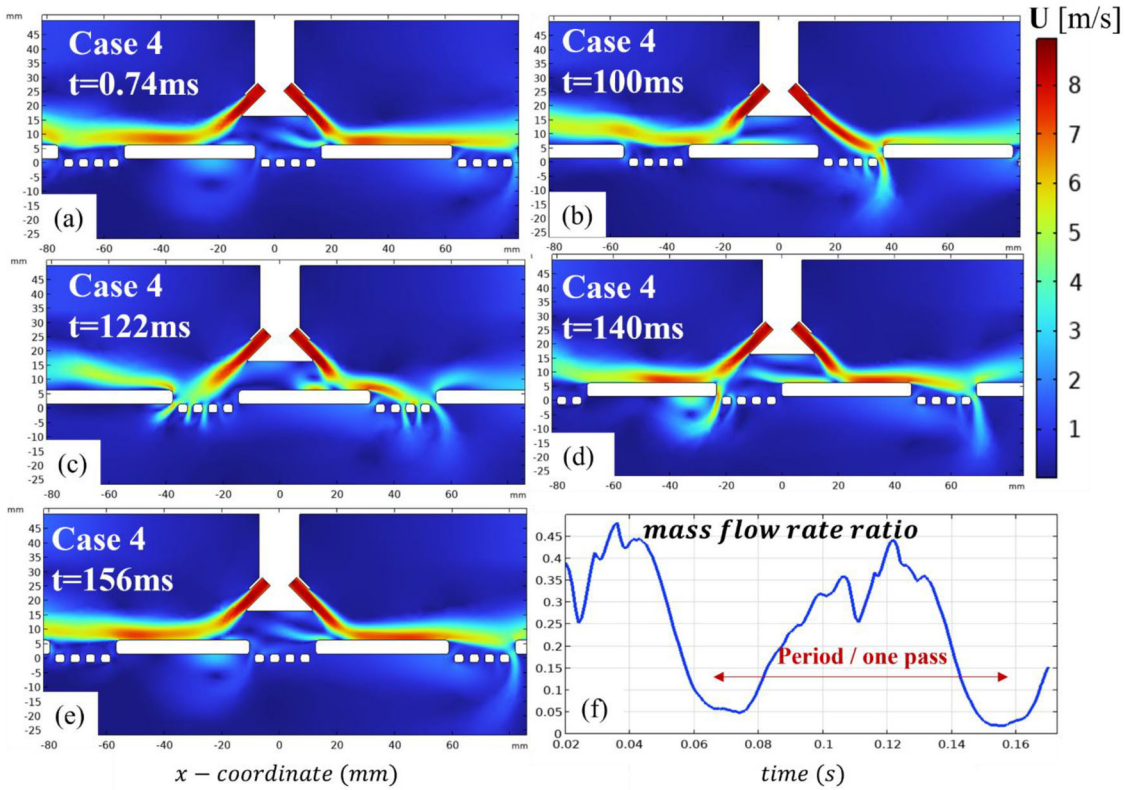

Figure 10. Case 4, u^*=0.1- (a-e) Flow field at specified times while the product in the middle passes (zoomed-in images); (f) *Mass flow rate ratio* with respect to time.

6.5. Stationary vs. Moving belt (Steady state vs. Transient study)

The summary of results for Cases 1-4 is tabulated in Table 1. The stationary study (Case 1) underpredicts the *mass flow rate ratio* of a moving belt without products (Case 3) by 13%. In addition, the stationary case with products at three different product locations (Case 2) shows that reattachment can happen on the product surface and product orientation affects the *mass flow rate ratio*. However, it does not convey the overall pattern of a moving surface's *mass flow rate ratio* as in Case 3.

In the transient cases, the shear stresses applied to the flow by the surface differ from that of the stationary cases due to surface motion. Therefore, the effect

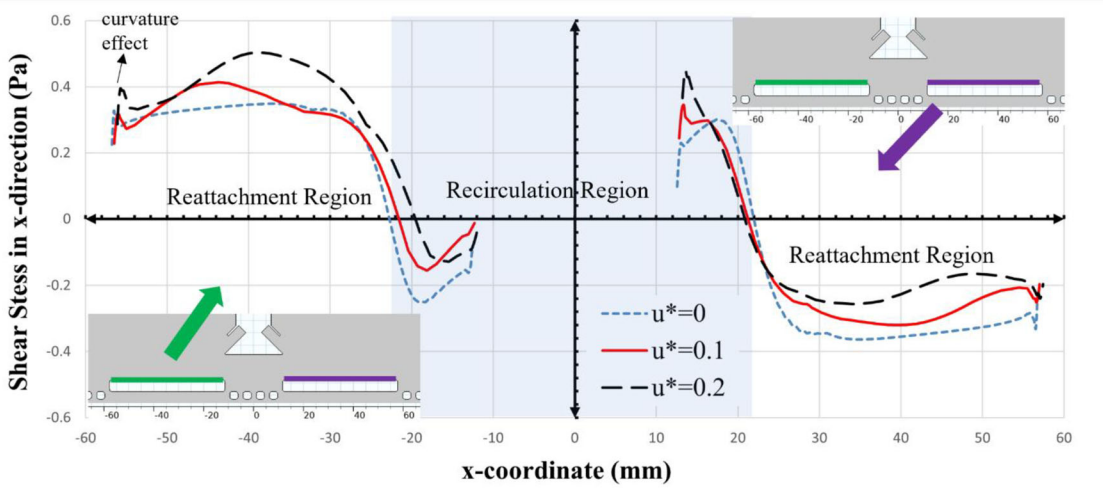

Figure 11. Shear stress in x-direction (τ_{w_x}) exerted by surface for Cases 2,4 and 5 or u^*=0, 0.1 and 0.2 at the instances where two products are aligned as shown in the pictures. For clarity, the recirculation and reattachment regions are displayed for u^*=0 case which slightly differ with other cases.

of surface movement on the flow field can also be captured in the shear stresses on the surface boundaries. Local shear stress in the x-direction (τ_{w_x}) at product surfaces is calculated based on Eq. (18) where, u_τ is friction velocity, u_x^T is the velocity in x-direction at the "wall" or product surface, and u^+ is the tangential dimensionless velocity.[57]

$$\tau_{w_x} = \rho u_\tau \frac{u_x^T}{u^+} \tag{18}$$

In Figure 11, the shear stresses in the x-direction applied by the product surface to the flow are plotted to compare the transient ($u^*\neq0$) and stationary (u^*=0) cases when two products are aligned with the flow reattachment locations. The numerical results presented in Figure 11 correspond to the product surface, and the effect of product curvature can be seen in the shear stress magnitudes for all cases at the two ends of the curves. The blue dashed line corresponds to Case 2, a stationary case. The transition from reattachment to the recirculation region can be identified when shear stress changes sign from positive to negative for the product on the left-hand side of the nozzle and vice-versa (displayed with a shaded region). As expected, the shear stresses are opposite to the flow near the product. On the same hand, the shear stresses in the reattachment region on the nozzle's left- and right-hand sides have similar magnitudes but in the opposite direction since the flows are in opposite directions. The direction of the flow changes in the recirculation region so as the direction of the shear stresses. (Note that the shear stress magnitudes on the nozzles' left- and right-hand sides are not identical because of the symmetry-breaking properties of the turbulent model, which can result in imperfect symmetries, which are aforementioned.)

In addition, for the transient cases, the surface movement affects the shear stress on two sides of the SJR nozzle differently. On the product on the left, the flow experiences higher shear stress than that of the right-hand side since this product is moving in the opposite direction to the flow, as expected. Moreover, the red line in Figure 11 corresponds to shear stresses for Case 4 (u^*=0.1), which follows a similar trend as the stationary case, but since the surface is moving in the x-direction, the shear stresses in the x-direction are generally elevated except for some portions of the recirculation region. (For instance, this exception occurs at x = 17-22mm. Due to the nature of the reattachment zone associated with the SJR nozzle flow field, the fluid is bi-directional, which results in the crossing of the curves in this region.) The other case plotted for u^*=0.2 follows the same trend with even higher stresses in the x-direction due to the higher surface velocity. In brief, although stationary cases can give estimates with relatively lower computational time, transient studies need to be performed to accurately capture the flow field of moving conveyor belts with and without products.

6.6. The effect of the presence of products

The summary of cases 1-4 is tabulated in Table 2, where Case 2 and Case 4 have products. Both stationary and transient cases showed clearly that the products significantly impact the SJR nozzle's flow field. Overall, the products decrease the mass flow escaping through the belt since they become obstacles and flow

Table 2. Summary of results for Cases 1–4.

	Mass flow rate ratio		
Case 1	61.6%		
Case 2	2.1-2.3	65.2%, 20.3% and 11.6% (respectively)	
Case 3	Max: 74.6%	Min: 68.8%	Average: 71%
Case 4	Max: 44.2%	Min: 1.8%	Average: 22.2%

reattaches on the product surface. In addition, the location of the products while traveling dictates the flow field, and escaping flow minimizes when two products align well with the nozzle exits when the flow reattaches on the product surface. Cases 1-4 results show that it is essential to include the products to accurately analyze and visualize the corresponding flow fields since products significantly alter the flow. Note that the results correspond to cases with a fixed product spacing based on available information to make this study more relevant to an industrial setting.

6.7. Case 5: The effect of belt speed

The effect of belt speed is investigated with Case 5, a transient study with moving conveyor belt and products with u^*=0.2. As aforementioned, the effect of shear stresses in the x-direction is plotted in Figure 11 for a given product orientation for three different belt speeds where the black dashed line corresponds to Case 5. As expected, Case 5 displays the highest shear stress in x-direction since Case 5 has the highest surface velocity compared to the other cases. In addition, the *mass flow rate ratio* of Case 5 is compared to Case 4 with u^*=0.1. Figure 12 shows the *mass flow rate ratio* with respect to displacement of products from the initial location at t = 0. The general trend of the *mass flow rate ratios* is similar for these two cases because geometries are similar. The comparison of Case 4 against Case 5 is tabulated in Table 3. On average over the averaging period or while the product in the middle passes below the SJR nozzle, Case 5, with doubled belt velocity, reveals 18.3% of the mass flow escaped under the belt, which is 17% lower than the baseline case (Case 4). In addition, the maximum *mass flow rate ratio* of Case 5 decreases by 30%. In brief, the results show that the escaping flow diminishes with the higher belt velocity of Case5 due to higher shear stresses in the x-direction.

6.8. Case 6: The effect of bottom SJR nozzle

The effect of placing an additional SJR nozzle to the bottom of the belt is studied in Case 6 because the flow loss (or escaping flow) is expected to be affected by the additional nozzle. In Case 6.1, the nozzles are symmetric about y = 0, and the flow field is given in

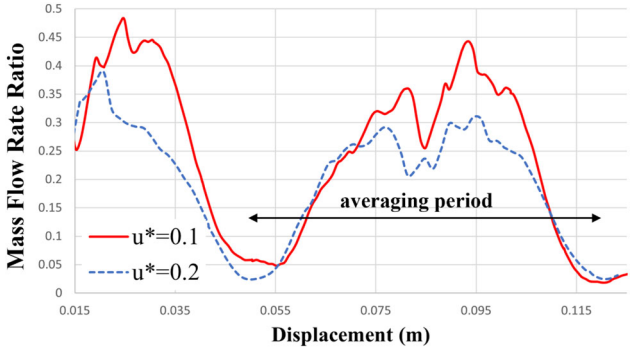

Figure 12. *Mass flow rate ratio* vs. displacement of products from the initial location at $t = 0$ with at two belt velocities corresponding u^*=0.1 and 0.2 (Case 4 and Case 5).

Table 3. The effect of belt speed on *mass flow rate ratio.*

		Mass flow rate ratio		
Case 4	u^*: 0.1	Max: 44.2%	Min: 1.8%	Average: 22.2%
Case 5	u^*: 0.2	Max: 30.9%	Min: 2.4%	Average: 18.3%

Figure 13 for specified instances while the product at the middle passes or within the averaging window where each instance shows a different product orientation. The results were obtained for each 1 ms and clearly show that both SJR nozzles have a reattachment region at all times regardless of the product position. These favorable results are expected because the nozzles are symmetric around the belt. The results clearly show that adding another SJR nozzle on the bottom would increase the impact of air since mass flow bleeding through the belt is minimal.

In an actual application, it may not be possible to have symmetric nozzles (or an array of nozzles). Therefore, Case 6.2 is studied where there is a 6 mm offset between the two nozzles. Figure 14 shows the flow field of this scenario at specified times, where each instance shows a different product orientation scenario. Case 6.2 displays a similar flow field trend compared to Case 6.1. However, since there is an offset, the reattachment regions do not align, resulting in slightly different flow fields. For example, at t = 130ms, the bottom nozzle's flow penetrates upwards through the belt, and the reattachment region is challenged but recovers with the next product at t = 130ms.

The *mass flow rate ratio* of Case 6.1 and Case 6.2 are plotted in Figure 15. Note that the denominator of Eq. (17), representing the total mass flow rate at the nozzle exits, is doubled due to having two nozzles. As expected, the *mass flow rate ratio* magnitudes are significantly lower than the previous cases without bottom nozzles, well below 10% and averages approximately −0.5%, as shown in Table 4. The

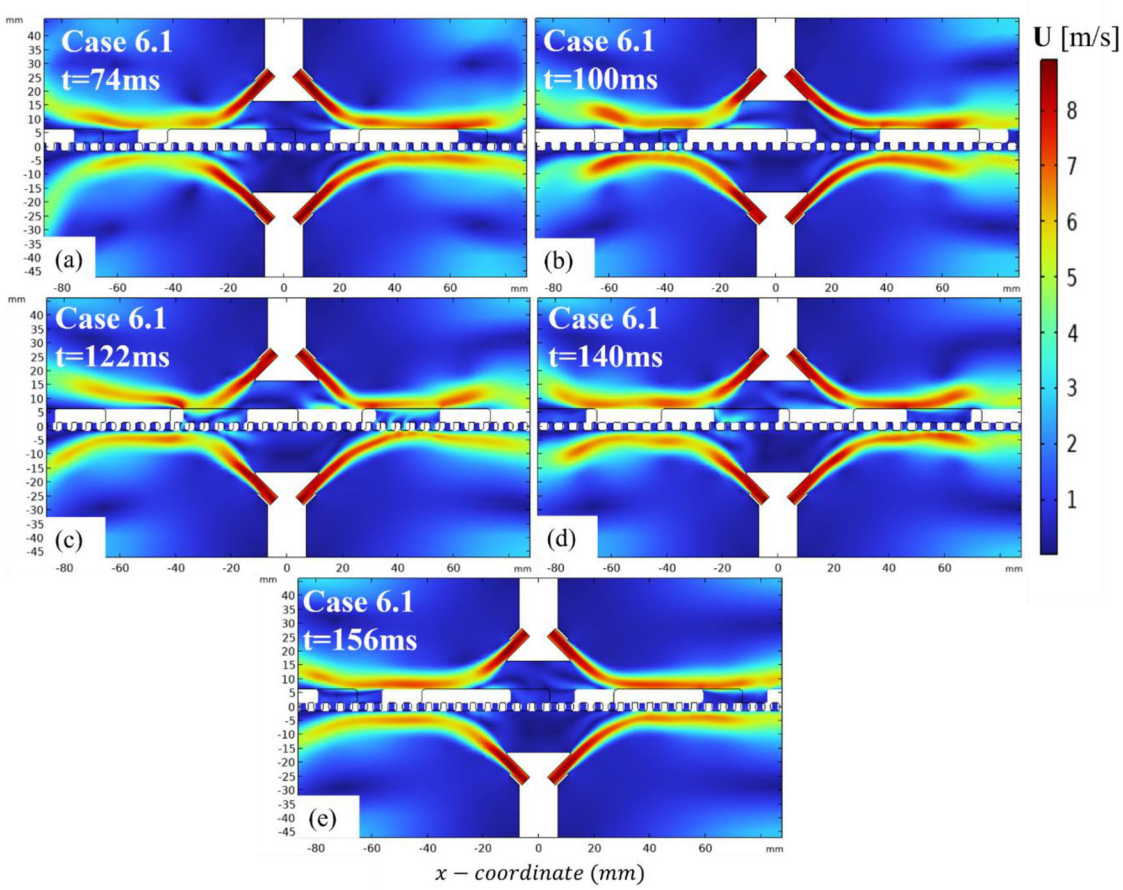

Figure 13. Case 6.1, u^*=0.1- SJR nozzles both top and bottom without offset between the two- (a-e) Flow field at specified times while the product in the middle passes (zoomed-in images) (The black lines showing in are watermarks displaying the initial position of the belt at $t = 0$s.).

negative sign indicates a net flow in the $+y$ direction since the escaping flow is defined in the $-y$ direction for previous cases. Case 6.1 and Case 6.2 have similar but shifted *mass flow rate ratio* curves because of the non-zero offset between the nozzles in Case 6.2. In Case 6.1, the *mass flow rate ratio* is generally non-zero because the geometry is not symmetric around $x = 0$ due to the products on the belt. Both *mass flow rate ratio* curves have a distinct pattern that is affected by the location of the products (i.e., time). For transient studies, the results indicate that the 6 mm offset between the nozzles do not significantly contribute to the flow field compared to the no-offset case, however the addition of bottom SJR nozzle creates a major difference in flow field in a positive way.

6.9. Forces exerted to the product

For sensitive or fragile products, peak forces acting on the products are crucial for product quality. This information can also be used to estimate if a product will lift off from the conveyor belt. Therefore, the forces on the middle (target) product are calculated by integrating the normal and shear forces acting on the product's surfaces as it passes through the SJR nozzle(s). All surfaces of the middle product are considered in integration, but the forces acting on the belt are not considered. Since the flow field analysis is 2 D, the resultant forces are given per unit width (in z-direction) of the product. The maximum magnitude of forces in $-x$, $+x$, $-y$ and $+y$ directions exerted on the product per unit width as the product travels are tabulated in Table 5. Note that, the tabulated results are the maximum magnitude values for each direction; so, the instances that correspond the tabulated values do not necessarily occur at the same time while the product travels.

As seen in Table 5, Case 4, the moving belt with products case (u^*=0.1) displays the highest maximum force magnitude in the -y direction with 0.33 N/m compared to the maximum force magnitudes in other directions. For example, for a square or circular product (estimation), the total peak force in the $-y$ direction can be calculated by multiplying 0.33 N/m by the width in the z-direction, 46.2 mm. This calculation results in 0.015 N. In addition, for all cases tabulated in Table 5,

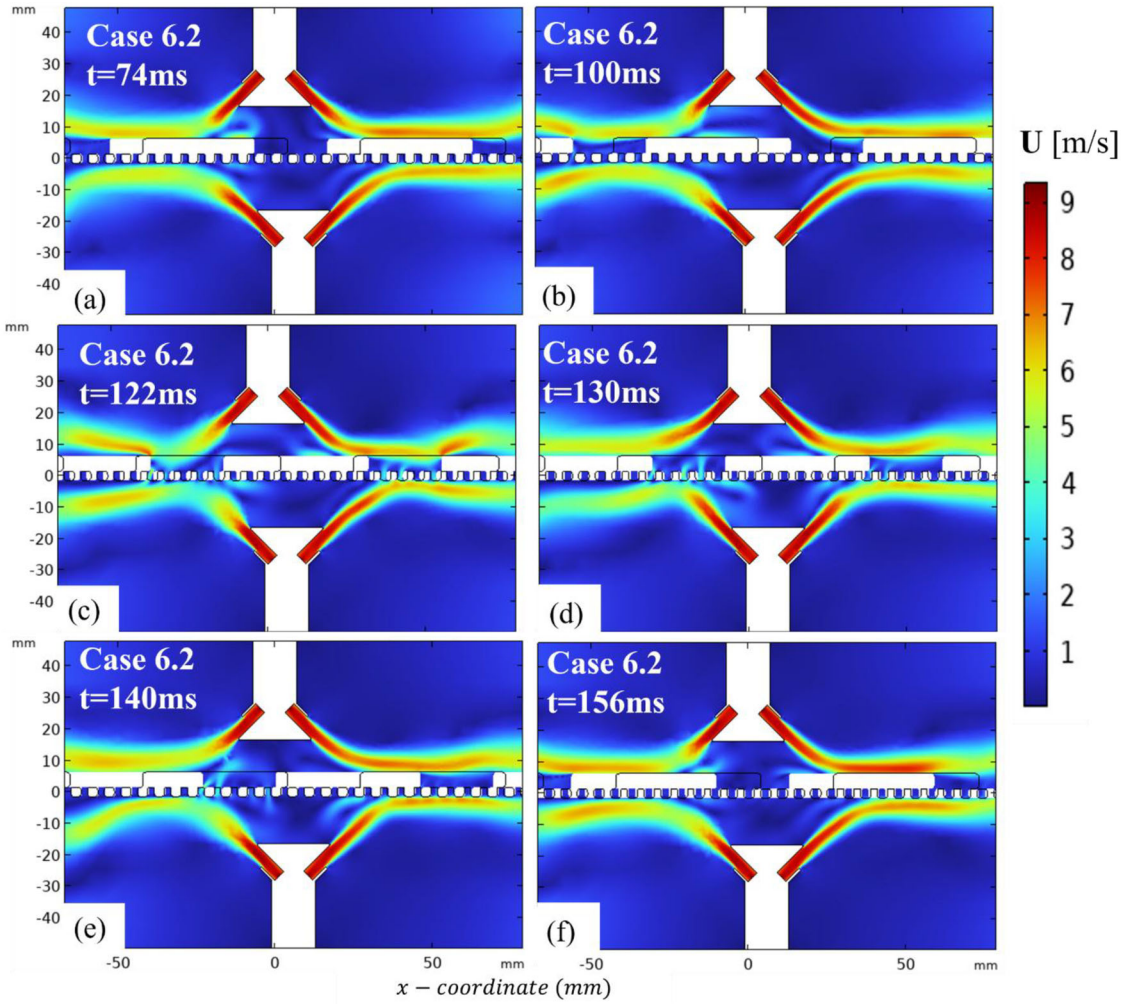

Figure 14. Case 6.2, u^*=0.1- SJR nozzles both top and bottom with 6 mm offset between the two- (a-f) Flow field at specified times while the product in the middle passes (zoomed-in images) (The black lines showing in (b-c) are watermarks displaying the initial position of the belt at $t = 0$s.).

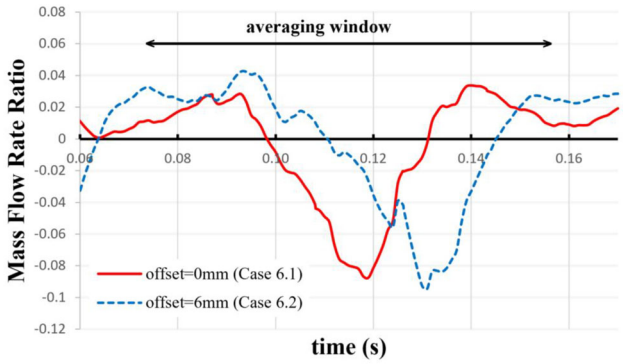

Figure 15. Case 6.1 and 6.2- *Mass flow rate ratio* vs time for cases with bottom SJR nozzle.

the highest maximum force magnitudes correspond to -y or +y directions rather than -x or x directions because of the nozzle(s)'s placement at the top (and bottom) side of the conveyor belt. With a higher belt velocity of u^*=0.2, max. force magnitude in the -y direction increases 24% compared to u^*=0.1 (Case 4). This is due to the higher mass flow that reattaches on the product surface since the mass bleeding through the belt is smaller with higher belt speed, as discussed previously. On the same hand, the max. force in + y direction decreases with higher belt velocity.

Case 4 and Case 6 have the same belt velocity, but Case 6 has an additional SJR nozzle on the bottom side of the conveyor belt. Case 6.1 and Case 6.2 have no and 6 mm lateral offset between the two nozzles. In Case 6.(1/2), the mass flow bleeding under the belt is very small because the *mass flow rate ratio* is below 1%. As seen in Figure 13 majority of the top SJR nozzle's flow for Case 6.1 reattaches on the product surface. Therefore, the maximum force in the -y direction increases compared to Case 4. Moreover, in Case 6.2, due to the lateral offset between the nozzles, the forces acting on the product surface slightly change. The dominant maximum force is in the +y-direction for Case 6.2 with 0.38 N/m.

Table 4. The effect of additional bottom SJR Nozzle on *mass flow rate ratio*.

		Mass flow rate ratio		
Case 4	Top nozzle only	Max: 44.2%	Min: 1.8%	Average: 22.2%
Case 6.1	Additional bottom nozzle with no offset	Max (magnitude): −8.7%	Min: 0%	Average: −0.5%
Case 6.2	Additional bottom nozzle with 6 mm offset	Max (magnitude): −9.4%	Min: 0%	Average: −0.4%

Table 5. Maximum magnitude of forces in −x, +x, −y and + y directions exerted to the product per unit product width (in *z*-direction) as product travels.

Case	Direction:	$-x$	$+x$	$-y$	$+y$	Unit
Case 4		0.01	0.03	0.33	0.21	N/m
Case 5		0.04	0.05	0.41	0.11	N/m
Case 6.1		0.04	0.05	0.38	0.26	N/m
Case 6.2		0.09	0.03	0.29	0.38	N/m

7. Conclusions

The impact of the reattachment surface characteristics on the performance of the slot jet reattachment (SJR) nozzle was studied. The reattachment surface was selected as a mesh-type conveyor belt with and without products. Turbulent fluid flow was theoretically modeled using the k-ε turbulence model for the SJR nozzle with 45° exit angle and other SJR nozzle parameters selected for the optimum conditions based on literature. Since this study was only concerned with analyzing the flow field of the SJR nozzle, energy rate equations were not solved; thus, heat transfer was not included. However, it is predicted that if the SJR flow reattachment occurs and there is little or no mass flow bleeding under the belt, the SJR nozzle's heat transfer performance on that perforated surface would be similar to that of a solid surface. The numerical predictions were validated with experimental data for stationary a surface under an SJR nozzle. The numerical study included: (1) Stationary surface; (2) stationary surface with products at three different locations; (3) transient study with moving surface; and (4) transient study with moving surface and products; (5) transient study with moving surface with products with higher surface speed; (6) transient study with moving surface and products with an additional SJR nozzle on the bottom of the surface.

The mass flow rate escapes through the belt was compared to the total mass flow rate at the nozzle inlets with a non-dimensional parameter called *mass flow rate ratio*. The higher the *mass flow rate ratio*, the greater the airflow bleeding through the belt and the lower the SJR nozzle's drying, heating, or cooling effectiveness. The major findings are summarized as follows:

- Stationary studies can help with preliminary results, but transient studies are critical to capture the shear force exerted by the moving belt (and products) and for accurate flow field results.
- While the conveyor belt moves with no load, 71% (temporal average) of the total flow is lost through the belt. However, when there are products on the belt, flow reattaches on the surface of the products and could decrease the mass loss down to 1.8% when two products are symmetrically aligned with the reattachment region. Therefore, products are crucial to include in the flow field analysis of an SJR nozzle.
- Overall, transient study (Case 4) results show that, on average, 22.2% of the mass flow is lost through the belt while a product passes underneath the nozzle.
- Doubling surface-to-jet flow velocity or the belt velocity results in 30% lower mass flow escape under the belt for the studied parameters (u^*=0.1 and 0.2).
- Shear stresses in *x*-direction (surface velocity direction) are compared for three different non-dimensional surface velocities (u^*=0,0.1,0.2). It was shown that flow experiences different shear stresses by the surface due to the surface movement, where the case with the highest surface velocity displayed highest shear stress in *x*-direction, as expected and vice versa. It was also shown that shear stresses downstream and upstream of the nozzle are affected by the surface motion differently due to the flow directionality with respect to the surface.
- Adding another SJR nozzle to the bottom, even if there is a 6mm offset between them, significantly improves the mass flow escaping under the belt—the *mass flow rate ratio* averages well below 1% for two SJR nozzle cases.
- As the product travels, the maximum magnitude of forces exerted on the middle product was reported for each direction. As expected, the forces in the -y and + y directions are much higher than those in the -x and + x directions.

Future studies will include the flow field analysis of an array of nozzles and heat transfer analysis to study the impact of reattachment surface on the heat transfer coefficients. In addition, the analysis of mesh-belt type (i.e., the distance between the belt pieces and looping of the belt) and product distribution (i.e., the blocking/perturbing effect of products and the effect of product spacing on the flow field) could be studied in the future.

Nomenclature

C_μ	Empirical constant in k-ε turbulence model (-)
$C_{\epsilon 1}$	Empirical constant in k-ε turbulence model (-)
$C_{\epsilon 2}$	Empirical constant in k-ε turbulence model (-)
P_k	Production term (kg/(m.s^3))
μ_T	Eddy (or turbulent) viscosity (kg/(m.s))
σ_k	Empirical constant in k-ε turbulence model (-)
τ_{w_x}	Local wall shear stress in x-direction (Pa)
b	SJR nozzle exit opening (m)
B	Constant, 5.2
D	Diameter or the width of the product (m)
D_h	Hydraulic diameter of the SJR nozzle, or 2b (m)
ε	Turbulent dissipation rate (m^2/s^3)
ILJ	Inline-jet
k	Turbulent kinetic energy (m^2/s^2)
κ_v	Von Karman constant, 0.41
n	Surface normal vector
P	Pressure (Pa)
Re	Reynolds number (-)
s	Product spacing (m)
SJ	Slot jet
SJR	Slot Jet Reattachment
t	Time (s)
th	Thickness of the product (m)
u	Air velocity in x-direction (m/s)
U	Velocity magnitude (m/s)
U	Velocity vector (m/s)
u^*	Surface-to-jet flow velocity (ub/ue) (-)
u^+	Tangential dimensionless velocity (-)
u_b	Velocity of the conveyor belt (m/s)
u_e	Average nozzle jet exit velocity (m/s)
u_x^T	Velocity in x-direction at the "wall" or product surface (m/s)
u_τ	Wall friction velocity (m/s)
v	Air velocity in y-direction (m/s)
X_p	Width of the nozzle's bottom plate (m)
Y_p	Nozzle-to-surface distance (m)
μ	Dynamic viscosity of air (kg/(m.s))
ρ	Air density (kg/m^3)

Funding

This study was financially supported by the US Department of Energy, Office of Advanced Manufacturing under Award Number DE-EE0009125, Massachusetts Clean Energy Center (MassCEC) and Center for Advanced Research in Drying (CARD), a US National Science Foundation Industry University Cooperative Research Center. CARD is located at Worcester Polytechnic Institute and the University of Illinois at Urbana-Champaign (co-site).

ORCID

Munevver Elif Asar http://orcid.org/0000-0001-7347-0204
Mengqiao Yang http://orcid.org/0000-0002-1449-2080

References

[1] Menon, A.; Stojceska, V.; Tassou, S. A. A Systematic Review on the Recent Advances of the Energy Efficiency Improvements in Non-Conventional Food Drying Technologies. *Trends Food Sci. Technol.* **2020**, *100*, 67–76. DOI: 10.1016/j.tifs.2020.03.014.

[2] Quadrennial Technology Review; US Department of Energy: September, **2015**.

[3] Tsotsas, E.; Mujumdar, A. S. *Modern Drying Technology*; John Wiley & Sons, **2011**. https://onlinelibrary.wiley.com/doi/book/10.1002/9783527631728

[4] Martin, H. Heat and Mass Transfer between Impinging Gas Jets and Solid Surfaces. In *Advances in Heat Transfer*; Elsevier, **1977**; Vol. 13, pp 1–60

[5] Baughn, J.; Shimizu, S. Heat Transfer Measurements from a Surface with Uniform Heat Flux and an Impinging Jet. *J Heat Transf. – Tran. of ASME* **1989**, *111*, 1096–1098. DOI: 10.1115/1.3250776.

[6] Zhao, W.; Kumar, K.; Mujumdar, A. Flow and Heat Transfer Characteristics of Confined Noncircular Turbulent Impinging Jets. *Drying Technol.* **2004**, *22*, 2027–2049. DOI: 10.1081/DRT-200034239.

[7] Colucci, D.; Viskanta, R. Effect of Nozzle Geometry on Local Convective Heat Transfer to a Confined Impinging Air Jet. *Exp. Therm. Fluid Sci.* **1996**, *13*, 71–80. DOI: 10.1016/0894-1777(96)00015-5.

[8] Brignoni, L. A.; Garimella, S. V. Effects of Nozzle-Inlet Chamfering on Pressure Drop and Heat Transfer in Confined Air Jet Impingement. *Int. J. Heat Mass Transf.* **2000**, *43*, 1133–1139. DOI: 10.1016/S0017-9310(99)00207-0.

[9] Lee, J.; Lee, S.-J. The Effect of Nozzle Aspect Ratio on Stagnation Region Heat Transfer Characteristics of Elliptic Impinging Jet. *Int. J. Heat Mass Transf.* **2000**, *43*, 555–575. DOI: 10.1016/S0017-9310(99)00167-2.

[10] Jiang, Y.; Xu, P.; Mujumdar, A. S.; Qiu, S.; Jiang, Z. A Numerical Study on the Convective Heat Transfer Characteristics of Pulsed Impingement Drying. *Drying Technol.* **2012**, *30*, 1056–1061. DOI: 10.1080/07373937.2012.683121.

[11] Kurnia, J. C.; Sasmito, A. P.; Tong, W.; Mujumdar, A. S. Energy-Efficient Thermal Drying Using Impinging-Jets with Time-Varying Heat Input–a Computational Study. *J. Food Eng.* **2013**, *114*, 269–277. DOI: 10.1016/j.jfoodeng.2012.08.029.

[12] Ekkad, S. V.; Singh, P. A Modern Review on Jet Impingement Heat Transfer Methods. *Trans. ASME, J. Heat Transf.* **2021**, *143*, 064001, 15. DOI: 10.1115/1.4049496.

[13] Katti, V.; Prabhu, S. Experimental Study and Theoretical Analysis of Local Heat Transfer Distribution between Smooth Flat Surface and Impinging Air Jet from a Circular Straight Pipe Nozzle. *Int. J. Heat Mass Transf.* **2008**, *51*, 4480–4495. DOI: 10.1016/j.ijheatmasstransfer.2007.12.024.

[14] Shiravi, A.; Mujumdar, A.; Kubes, G. Numerical Study of Heat Transfer and Fluid Flow in Multiple Turbulent Impinging Jets. *Drying Technol.* **1995**, *13*, 1359–1375. DOI: 10.1080/07373939508917027.

[15] Liu, Z.-L.; Bai, J.-W.; Yang, W.-X.; Wang, J.; Deng, L.-Z.; Yu, X.-L.; Zheng, Z.-A.; Gao, Z.-J.; Xiao, H.-W. Effect of High-Humidity Hot Air Impingement Blanching (HHAIB) and Drying Parameters on Drying Characteristics and Quality of Broccoli

Florets. *Drying Technol.* **2019**, *37*, 1251–1264. DOI: 10.1080/07373937.2018.1494185.

[16] Liu, Z.-L.; Bai, J.-W.; Wang, S.-X.; Meng, J.-S.; Wang, H.; Yu, X.-L.; Gao, Z.-J.; Xiao, H.-W. Prediction of Energy and Exergy of Mushroom Slices Drying in Hot Air Impingement Dryer by Artificial Neural Network. *Drying Technol.* **2020**, *38*, 1959–1970. DOI: 10.1080/07373937.2019.1607873.

[17] Ai, Z.; Xiao, H.; Zhang, Y.; Lei, D.; Peng, Z.; Li, M.; Liu, Y. Effect of Hot Air Impingement Drying on Drying Behavior, Volatile Components Profile, Shell Burst Ratio, Flavonoid Contents, Microstructure of Amomum Villosum Fruits. *Drying Technol.* **2022**, 1–15. DOI: 10.1080/07373937.2022.2087184.

[18] Boy, V.; Liu, X.; Chamaa, M.-A.; Lemée, Y.; Sabourin, C.; Lendormi, T.; Lanoisellé, J.-L. Air Impingement Drying of Digestate: Experimental and Modelling Study. *Chem. Eng. Res. Des.* **2019**, *146*, 436–448. DOI: 10.1016/j.cherd.2019.03.033.

[19] Khatir, Z.; Paton, J.; Thompson, H.; Kapur, N.; Toropov, V. Optimisation of the Energy Efficiency of Bread-Baking Ovens Using a Combined Experimental and Computational Approach. *Appl. Energy* **2013**, *112*, 918–927. DOI: 10.1016/j.apenergy.2013.02.034.

[20] Yang, M.; Yagoobi, J.; Tilley, B. Heat Transfer Enhancement of Ionic Wind Assisted Slot Jet Reattachment Nozzle: A Numerical Study. *Trans. ASME, J. Heat Transf.* **2022**, *144*, 072301. 8. DOI: 10.1115/1.4054156.

[21] Seyed-Yagoobi, J. Enhancement of Heat and Mass Transfer with Innovative Impinging Jets. *Drying Technol.* **1996**, *14*, 1173–1196. DOI: 10.1080/07373939608917143.

[22] Page, R.; Seyed-Yagoobi, J. A New Concept for Air or Vapor Impingement Drying. *Tappi J.* **1990**, *73*, 229–234.

[23] Peper, F.; Leiner, W.; Fiebig, M. Impinging Radial and Inline Jets: A Comparison with Regard to Heat Transfer, Wall Pressure Distribution, and Pressure Loss. *Exp. Therm. Fluid Sci.* **1997**, *14*, 194–204. DOI: 10.1016/S0894-1777(96)00066-0.

[24] Page, R.; Carbone, J.; Ostowari, C. Radial Jet Reattachment Force. *Exp. Fluids* **1990**, *8*, 297–298. DOI: 10.1007/BF00187233.

[25] Seyed-Yagoobi, J.; Page, R. H. Slot Jet Reattachment Nozzle and Method of Operation, **2000**, #6142391.

[26] Narayanan, V.; Seyed-Yagoobi, J.; Page, R. Heat Transfer Characteristics of a Slot Jet Reattachment Nozzle. *J Heat Transf. – Trans. ASME* **1998**, *120*, 348–356. DOI: 10.1115/1.2824255.

[27] Alam, S. A.; Seyed-Yagoobi, J.; Narayanan, V.; Page, R. Drying Characteristics of Slot Jet Reattachment Nozzle and Comparison with a Slot Jet Nozzle. *Drying Technol.* **1998**, *16*, 1585–1607. DOI: 10.1080/07373939808917481.

[28] Farzad, M.; El Ferouali, H.; Kahraman, O.; Yagoobi, J. Enhancement of Heat Transfer and Product Quality Using Jet Reattachment Nozzles in Drying of Food Products. *Drying Technol.* **2022**, *40*, 352–370. DOI: 10.1080/07373937.2020.1804927.

[29] Farzad, M.; Yagoobi, J. Drying of Moist Cookie Doughs with Innovative Slot Jet Reattachment Nozzle. *Drying Technol.* **2021**, *39*, 268–278. DOI: 10.1080/07373937.2020.1729173.

[30] Nienke, T.; Embrechts, H.; Kwade, A.; Eggerath, D. Experimental and Numerical Investigation of the Influence of Nozzle Design on the Industrial Convection Drying of Thin Films. *Drying Technol.* **2022**, *40*, 2685–2695. DOI: 10.1080/07373937.2021.1954941.

[31] Zumbrunnen, D. Convective Heat and Mass Transfer in the Stagnation Region of a Laminar Planar Jet Impinging on a Moving Surface. *J Heat Transf. – Trans. ASME* **1991**, *113*, 563–570. DOI: 10.1115/1.2910603.

[32] Shah, S. A Numerical Study of Heat Transfer from an Array of Jets Impinging on a Flat Moving Surface. *Trans. ASME, J. Heat Transf.* **2022**, *144*, 042302. 11. DOI: 10.1115/1.4053451.

[33] Chen, J.; Wang, T.; Zumbrunnen, D. Numerical Analysis of Convective Heat Transfer from a Moving Plate Cooled by an Array of Submerged Planar Jets. *Num. Heat Transf., Part A: Appl.* **1994**, *26*, 141–160. DOI: 10.1080/10407789408955985.

[34] Chattopadhyay, H.; Saha, S. K. Turbulent Flow and Heat Transfer from a Slot Jet Impinging on a Moving Plate. *Int. J. Heat Fluid Flow* **2003**, *24*, 685–697. DOI: 10.1016/S0142-727X(03)00062-6.

[35] Chattopadhyay, H. Effect of Surface Motion on Transport Processes Due to Circular Impinging Jets—A Numerical Study. *Drying Technol.* **2006**, *24*, 1347–1351. DOI: 10.1080/07373930600951117.

[36] Kadiyala, P. K.; Chattopadhyay, H. Numerical Simulation of Transport Phenomena Due to Array of Round Jets Impinging on Hot Moving Surface. *Drying Technol.* **2017**, *35*, 1742–1754. DOI: 10.1080/07373937.2016.1275672.

[37] Huang, P.; Mujumdar, A.; Douglas, W. Numerical Prediction of Fluid Flow and Heat Transfer under a Turbulent Impinging Slot Jet with Surface Motion and Crossflow. *ASME Paper* **1984**, 1–8.

[38] Raju, K. S.; Schlünder, E. Heat Transfer between an Impinging Jet and a Continuously Moving Flat Surface. *Wärme-Und Stoffübertragung* **1977**, *10*, 131–136. DOI: 10.1007/BF01682706.

[39] Senter, J.; Solliec, C. Flow Field Analysis of a Turbulent Slot Air Jet Impinging on a Moving Flat Surface. *Int. J. Heat Fluid Flow* **2007**, *28*, 708–719. DOI: 10.1016/j.ijheatfluidflow.2006.08.002.

[40] Chen, J.; Lau, S. K.; Chen, L.; Wang, S.; Subbiah, J. Modeling Radio Frequency Heating of Food Moving on a Conveyor Belt. *Food Bioprod. Process.* **2017**, *102*, 307–319. DOI: 10.1016/j.fbp.2017.01.009.

[41] Kangarluei, A. R., Heat and Mass Transfer in Industrial Biscuit Baking Oven and Effect of Temperature on Baking Time. *J. Heat Mass Transf. Res.* **2015**, *2*, 79–90. DOI: 10.22075/JHMTR.2015.343.

[42] El-Mesery, H. S.; Mwithiga, G. Performance of a Convective, Infrared and Combined Infrared-Convective Heated Conveyor-Belt Dryer. *J. Food Sci. Technol.* **2015**, *52*, 2721–2730. DOI: 10.1007/s13197-014-1347-1.

[43] Baik, O.; Marcotte, M.; Castaigne, F. Cake Baking in Tunnel Type Multi-Zone Industrial Ovens Part I. Characterization of Baking Conditions. *Food Res. Int.* **2000**, *33*, 587–598. DOI: 10.1016/S0963-9969(00)00095-8.

[44] Baik, O.; Marcotte, M.; Castaigne, F. Cake Baking in Tunnel Type Multi-Zone Industrial Ovens Part II. Evaluation of Quality Parameters. *Food Res. Int.* **2000**, *33*, 599–607. DOI: 10.1016/S0963-9969(00)00096-X.

[45] Xue, J.; Walker, C. Humidity Change and Its Effects on Baking in an Electrically Heated Air Jet Impingement Oven. *Food Res. Int.* **2003**, *36*, 561–569. DOI: 10.1016/S0963-9969(02)00221-1.

[46] Zareifard, M.; Boissonneault, V.; Marcotte, M. Bakery Product Characteristics as Influenced by Convection Heat Flux. *Food Res. Int.* **2009**, *42*, 856–864. DOI: 10.1016/j.foodres.2009.03.008.

[47] Farzad, M.; Yagoobi.; J.; In *Effect of Impingement Surface Velocity on Slot Jet and Slot Jet Reattachment Nozzles' Flow Field*, ASME International Mechanical Engineering Congress and Exposition, Salt Lake City, Utah, USA, January 21, 2020; American Society of Mechanical Engineers: Salt Lake City, Utah, USA, **2019**; p V007T08A025 (6 pages).

[48] Farzad, M.; Yagoobi, J. In *Convective Air Drying of Stationary and Moving Moist Porous Medium With Slot Jet Reattachment Nozzle: A Numerical Study*, ASME International Mechanical Engineering Congress and Exposition, Virtual, Online, February 16, 2021; American Society of Mechanical Engineers: Virtual, Online, **2020**; p V011T11A033 (8 pages).

[49] COMSOL Multiphysics® 6.0 Release Highlights. https://www.comsol.com/release/6.0?gclid=CjwKCAjwm8WZBhBUEiwA178UnDBcgbY41JhxsU-QHK4aS1n8foGmimwo62q44gInoIOrQQA9y6J1kIR-oCXMwQAvD_BwE. (accessed 26 September **2022**.

[50] COMSOL The k-ε Turbulence Model. https://doc.comsol.com/5.5/doc/com.comsol.help.cfd/cfd_ug_fluidflow_single.06.088.html (accessed 5 May **2022**).

[51] Farzad, M.; El Ferouali, H.; Asar, M. E.; Yagoobi, J. Enhancement of Drying of Food Products with Slot Jet Reattachment Nozzles in a Convective Oven with a Moving Belt. In *22nd International Drying Symposium, Worcester, Massachusetts, USA*, **2022**; pp 1–7.

[52] Narayanan, V.; Seyed-Yagoobi, J.; Page, R.; Alam, S. Effect of Exit Angle on the Heat Transfer Characteristics of a Slot Jet Reattachment Nozzle and Its Comparison to a Slot Jet Nozzle. *ASME Natl. Heat Transf. Conf.* **1997**, *347*, 119–128.

[53] COMSOL Segregated. https://doc.comsol.com/5.5/doc/com.comsol.help.comsol/comsol_ref_solver.27.167.html. (accessed 9 November 2022).

[54] COMSOL PARSIDO 7.2. https://pardiso-project.org/. (accessed November 9 2022).

[55] Crawford, J. D.; Knobloch, E. Symmetry and Symmetry-Breaking Bifurcations in Fluid Dynamics. *Annu. Rev. Fluid Mech.* **1991**, *23*, 341–387. DOI: 10.1146/annurev.fl.23.010191.002013.

[56] Oberlack, M. Symmetries and Invariant Solutions of Turbulent Flows and Their Implications for Turbulence Modelling. In *Theories of Turbulence*, Springer: Vienna, **2002**; pp 301–366

[57] White, F. *Viscous Fluid Flow*. 3rd ed.; McGraw Hill Education: New York, NY, **2011**.